

On-Chip Ni–Zn Microbattery Based on Hierarchical Ordered Porous Ni@Ni(OH)₂ Microelectrode with Ultrafast Ion and Electron Transport Kinetics

Zhimeng Hao, Lin Xu, Qin Liu, Wei Yang, Xiaobin Liao, Jiashen Meng, Xufeng Hong, Liang He,* and Liqiang Mai*

On-chip microbatteries have attracted growing attention due to their great feasibility for integration with miniaturized electronic devices. Nevertheless, it is difficult to get both high energy/power densities in microbatteries. An increase in the thickness of microelectrodes may help to boost the areal energy density of device, yet it often leads to terrible sacrifice in its power density due to the longer electron and ion diffusion distances. In this work, a quasi-solid-state on-chip Ni–Zn microbattery is designed based on a hierarchical ordered porous (HOP) Ni@Ni(OH)₂ microelectrode, which is developed by an in situ anodizing strategy. The fabricated microelectrode can optimize ion and electron transport simultaneously due to its interconnected ordered macropore–mesopore network and high electron conductivity. As the thickness of microelectrode increases, the areal energy density of HOP Ni@Ni(OH)₂ microelectrode shows an ascending trend with negligible sacrifice in power density and rate performance. Impressively, this Ni–Zn microbattery achieves excellent energy/power densities (0.26 mW h cm⁻², 33.8 mW cm⁻²), outperforming most previous reported microenergy storage devices. This study may provide new direction in high-performance and highly safe microenergy storage units for next-generation highly integrated microelectronics.

high energy/power densities, high rate capability, and long service lifetime.^[1] On-chip micropower sources are essential for the future development of smart medical implants, artificial intelligence robots, microscale wireless sensor networks, and other self-powered microsystems.^[2] In the past decade, on-chip microbatteries (MBs) have attracted tremendous attention because of their ultrahigh energy density and great feasibility for integration into miniaturized devices.^[3] Therefore, on-chip MBs are deemed to be highly promising candidates for integrating into amounts of electronic microdevices/systems. In most of the applications, the combination of high energy/power densities and rate capability is required. Nevertheless, it is challenging to get high energy/power densities and rate capability simultaneously in MBs owing to footprint restrictions.^[4] As one of the commercial configurations, thin-film MBs are widely adopted owing to their relatively high-power supply and

1. Introduction

The recent technological trend in electronics industry toward small scale and highly integrated electronic devices has stimulated ever-growing demand for on-chip micropower sources with outstanding electrochemical performances, such as

tremendous reduced thickness compared with traditional batteries.^[5] However, in order to provide sufficient energy, thin-film MBs usually require large footprints, due to their low active material loading per unit area.^[6] Increasing the thickness of microelectrodes may help to boost the active material loading, so as to get higher areal energy density of device. But the longer electron and ion diffusion distances often result in a decreased power density and worse rate performance.^[7] Searching for approaches to fabricate on-chip MBs with high energy/power densities and rate capability simultaneously is an urgent and challenging mission.

To overcome these challenges, the design of the microelectrodes structure is particularly important. MB based on 3D microstructured electrodes is one of the promising designs for achieving high energy/power densities and rate capability in a given footprint area simultaneously.^[8] As one of the typical microelectrode configurations, microelectrodes based on high-aspect-ratio micropillar structures have been developed by polymer pyrolysis,^[9] electrodeposition,^[10] and so on. Although this type of microelectrodes can achieve enhanced energy density compared with 2D microelectrodes due to higher material loading, the solid structure is still suffering from

Z. M. Hao, Prof. L. Xu, Q. Liu, W. Yang, X. B. Liao, J. S. Meng, X. F. Hong, Prof. L. He, Prof. L. Q. Mai
State Key Laboratory of Advanced Technology for Materials Synthesis and Processing
International School of Materials Science and Engineering
Wuhan University of Technology
Wuhan 430070, P. R. China
E-mail: hel@whut.edu.cn; mlq518@whut.edu.cn

Prof. L. He
Department of Materials Science and NanoEngineering
Rice University
Houston, TX 77005, USA

 The ORCID identification number(s) for the author(s) of this article can be found under <https://doi.org/10.1002/adfm.201808470>.

DOI: 10.1002/adfm.201808470

decreased power density owing to the inefficient electron and ion transport. 3D order macroporous (3DOM) microelectrodes can provide short ion transport distance and efficient electron pathway.^[11] Attributed to these merits, MBs based on 3DOM microelectrodes can realize high energy/power densities and rate capability simultaneously. 3D mesostructured microelectrodes possess all the merits of 3DOM microelectrodes and higher specific surface area, which makes them more potential for achieving high energy/power densities and rate capability.^[12] However, majority of approaches to synthesize 3D mesostructured electrodes, such as hydrothermal method, are difficult to be applied to on-chip MBs. Although there are some advances in MBs, the development of MBs based on 3D mesostructured microelectrodes is still in the initial stage.^[4b] In addition, although vast majority of small-scale electronic devices rely on lithium-ion microbatteries (LIMBs) to get their energy supply, the wide application of LIMBs is severely limited by their high cost, complex encapsulations, especially safety issues.^[13] Aqueous nickel–zinc (Ni–Zn) batteries are considered as promising alternatives to LIBs due to their relatively high power density, facile encapsulations and intrinsic safety, although their cycling stability is often unsatisfactory due to the formation of dendrites and passivation of zinc electrode.^[14] Integrating Ni–Zn system into MBs is significant for the development of safe MBs with high performance. However, to the best of our knowledge, no publications have been concentrated on the on-chip Ni–Zn MBs based on interdigital mesostructured microelectrodes.

Herein, we constitute a quasi-solid-state on-chip Ni–Zn MB based on an interdigital hierarchical ordered porous (HOP) Ni@Ni(OH)₂ microelectrode. The HOP Ni@Ni(OH)₂ microelectrode has a HOP core–shell structure with HOP Ni skeleton as core and a layer of highly active Ni(OH)₂ as shell. The HOP Ni skeleton is fabricated via a colloidal templating

strategy combining with the electrodeposition of Ni on a Ti/Au current collector and the Ni(OH)₂ layer is in situ grown on the surface of HOP Ni skeleton by facile anodizing. This design can optimize ion and electron transport simultaneously. In details, it provides i) large surface area for highly active Ni(OH)₂ loading, ii) ordered macropores for electrolyte-ion accessibility, iii) interconnected mesopores for efficient ion transport, and (iv) high electron conductivity to promote electron transport. As a consequence, the HOP Ni@Ni(OH)₂ microelectrode shows an enhanced areal capacity of 302.9 $\mu\text{A h cm}^{-2}$ at 1 mA cm^{-2} and a better rate performance (65.81% capacity retention at 50 mA cm^{-2}) than those of Ni@Ni(OH)₂ derived from a solid Ni (S Ni@Ni(OH)₂). Exhilaratingly, as thickness of the microelectrodes increases, the areal energy density of HOP Ni@Ni(OH)₂ microelectrode shows an ascending trend with a weeny sacrifice in areal power density. As a demonstration, a quasi-solid-state on-chip Ni–Zn MB with gel electrolyte is assembled. The fabricated quasi-solid-state on-chip Ni–Zn MB exhibits a considerable capacity of 150.1 $\mu\text{A h cm}^{-2}$ with prominent long-term stability (74.6% capacity retention after 1800 cycles). More importantly, it achieves ultrahigh energy (0.26 mW h cm^{-2} , 0.12 W h cm^{-3}) and power densities (33.8 mW cm^{-2} , 15.8 W cm^{-3}). The areal/volumetric energy/power densities are considerably superior to most reported microenergy storage device.

2. Results and Discussion

2.1. Morphology and Structure

The fabrication process of the quasi-solid-state on-chip Ni–Zn MB is illustrated in **Figure 1**. First, interdigital Ti/Au current collectors were obtained on a Si/SiO₂ substrate through photolithography and physical vapor deposition (PVD). Then, the

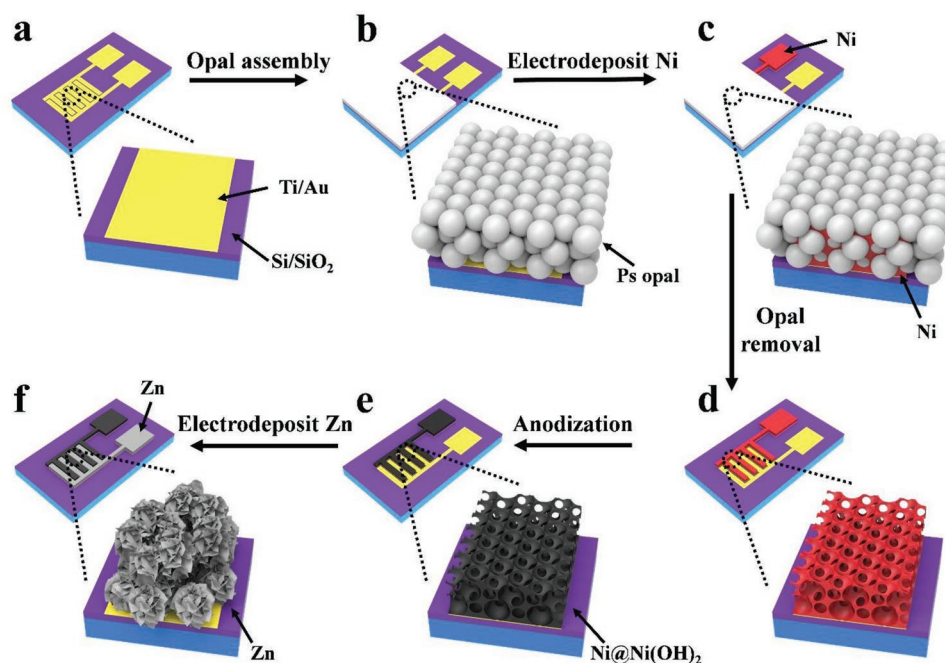


Figure 1. Schematic illustration of the fabrication process of HOP Ni–Zn MBs.

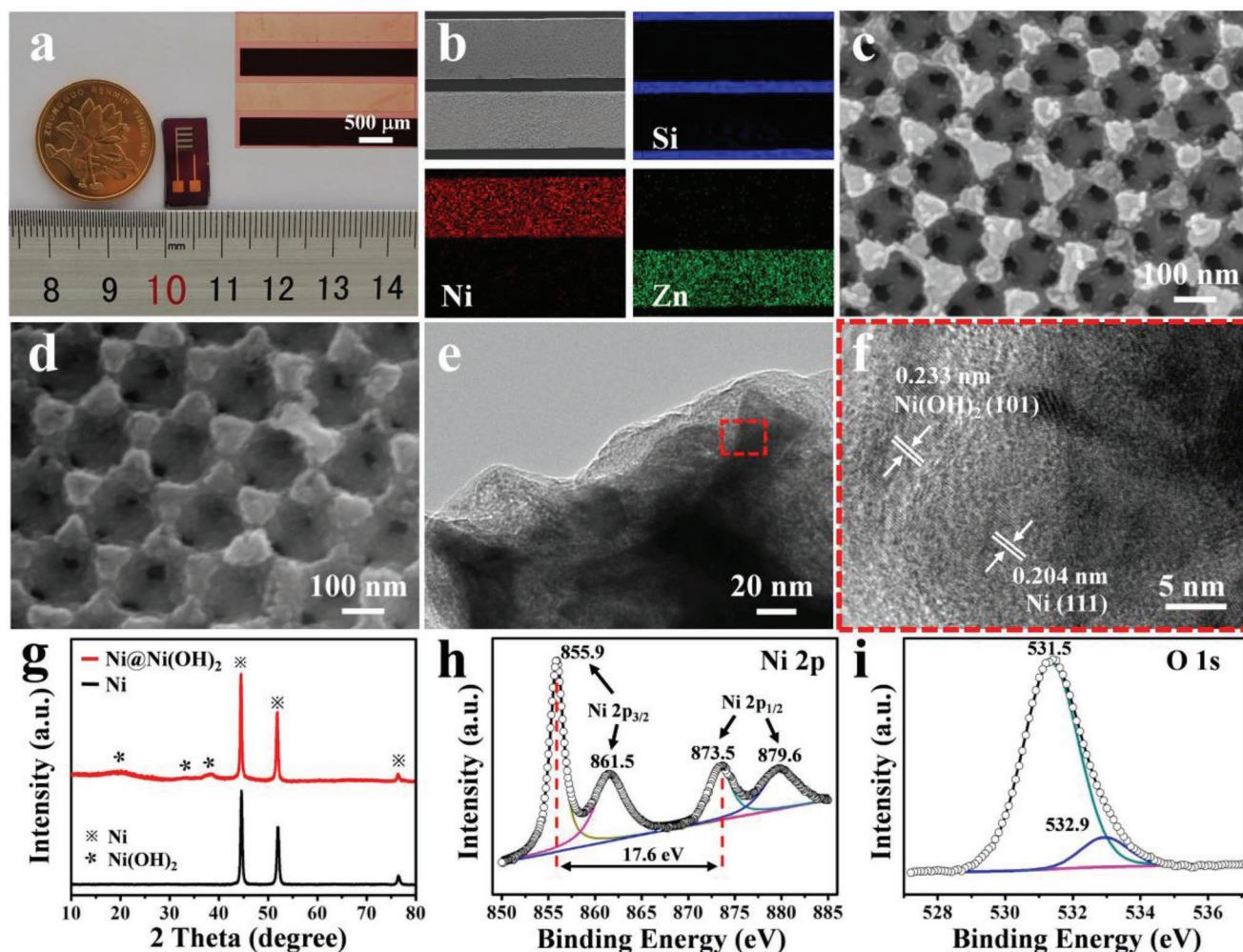


Figure 2. a) Digital camera image of HOP Ni–Zn MB; the inset is the corresponding magnified bright-field optical image. b) EDS mapping images of Si, Ni, and Zn elements of interdigital microelectrodes. c) SEM image of the HOP Ni@Ni(OH)₂ microelectrode. d) SEM image of the cross-section of HOP Ni@Ni(OH)₂ microelectrode. e, f) TEM and HRTEM images of HOP Ni@Ni(OH)₂ microelectrode. g) XRD spectra of HOP Ni@Ni(OH)₂ microelectrode and HOP Ni skeleton. XPS spectra of h) Ni 2p and i) O 1s of HOP Ni@Ni(OH)₂ microelectrodes.

polystyrene (PS) template was assembled on the substrate via vertical deposition method (Figure S1, Supporting Information). Next, nickel metal was electrodeposited through the PS template. After that, the template was removed by methylbenzene to obtain a rationally designed HOP Ni skeleton (Figure S2, Supporting Information). Subsequently, Ni(OH)₂ was in situ formed by anodizing the surface of HOP Ni skeleton to obtain HOP Ni@Ni(OH)₂ microelectrode. As a contrast, a S Ni@Ni(OH)₂ microelectrode was fabricated without the PS template. Initially, the microelectrode is stacked from numerous lumpy Ni blocks (Figure S3, Supporting Information). In addition, there are some pores and tiny cracks between the Ni blocks. After anodizing, the surface of Ni was converted into Ni(OH)₂ and became rough (Figure S4, Supporting Information). On the other hand, Zn microelectrode as the anode was achieved through a facile electrodeposition. The scanning electron microscope (SEM) images (Figure S5a–c, Supporting Information) of the Zn microelectrode show that the Zn nanosheets are distributed uniformly on the current collector. The X-ray diffraction (XRD) pattern (Figure S5d, Supporting Information)

of Zn microelectrode demonstrates that the characteristic peaks are well indexed to Zn (JCPDS No. 03-065-5973).

The fabricated on-chip MB has a small footprint area less than a coin (Figure 2a). The optical image (inset in Figure 2a) of the interdigital microelectrodes shows that the regular width of each interdigital microelectrode and the interspace between microelectrodes are 400 and 100 μm, respectively. The SEM image and the corresponding energy-dispersive spectroscopy (EDS) mapping images (Figure 2b) of two neighbor interdigital microelectrodes clearly verify the homogeneous distribution of Si, Ni, and Zn elements, which indicates that the geometrical configuration of finely patterned microelectrodes is reserved well after anodizing process. Due to the in situ growth of Ni(OH)₂, the surface of HOP Ni@Ni(OH)₂ microelectrode becomes more rough than that of HOP Ni skeleton (Figure 2c, d). Impressively, the HOP structure is reserved and the diameter of the interconnect mesopores between the macropores is about 25–45 nm. For a more detailed understanding of the growth of Ni(OH)₂, transmission electron microscopy (TEM) and high resolution

transmission electron microscopy (HRTEM) were investigated (Figure 2e,f). The lattice spacings of 0.204 and 0.233 nm correspond well to the (111) plane of Ni (JCPDS No. 01-089-7128) and the (101) plane of Ni(OH)₂ (JCPDS No. 00-014-0117) can be obviously observed, respectively. In order to further investigate the composition of HOP Ni@Ni(OH)₂, XRD and X-ray photoelectron spectroscopy (XPS) analyses were employed. Obviously, besides the characteristic peaks from Ni skeleton, three characteristic peaks of Ni(OH)₂ can be observed in the XRD spectra of the HOP Ni@Ni(OH)₂ microelectrode, indicating that a pure Ni(OH)₂ layer is successfully conducted on the surface of the microelectrode (Figure 2g). XPS studies further confirmed the formation of the HOP Ni@Ni(OH)₂. Evidently, excluding the C peak coming from the reference carbon, only O and Ni elements can be observed in HOP Ni@Ni(OH)₂ (Figure S6, Supporting Information). From the Ni 2p high-resolution spectrum (Figure 2h), two typical peaks at 873.5 and 855.9 eV are consistent well with Ni 2p_{1/2} and Ni 2p_{3/2} levels, respectively. The spin-energy separation of 17.6 eV, a feature of a Ni(OH)₂ phase, further indicates the presence of Ni(OH)₂.^[15] The O 1s high-resolution spectrum (Figure 2i) shows two oxygen contributions. The major peak at 531.3 eV is associated with oxygen in OH⁻ groups coming from Ni(OH)₂, and the tiny peak at 532.9 eV is assigned to adsorbed oxygen species at or near the surface.^[16] All of these results demonstrate that the microelectrode has a HOP core-shell architecture with HOP Ni as core and a layer of Ni(OH)₂ as shell.

2.2. The Electrochemical Performance of HOP Ni@Ni(OH)₂ Microelectrodes

To explore the effect of thickness of HOP Ni@Ni(OH)₂ microelectrode and S Ni@Ni(OH)₂ microelectrode on the electrochemical performance, the microelectrodes with different thicknesses were prepared (denoted as HOP Ni@Ni(OH)₂-X and S Ni@Ni(OH)₂-X, respectively. X presents the thickness of microelectrode). The electrochemical performances of these microelectrodes were evaluated in a three-electrode system with 1 M KOH aqueous electrolyte. Cyclic voltammograms (CV) curves (Figure S7, Supporting Information) of HOP Ni@Ni(OH)₂-X microelectrodes and S Ni@Ni(OH)₂-X microelectrodes at various scan rates show one set of redox peaks, which corresponds to the electrochemical reaction: 2 Ni(OH)₂ + 2 OH⁻ ⇌ 2 NiOOH + 2 H₂O + 2 e⁻. The specific capacities of those HOP Ni@Ni(OH)₂-X microelectrodes at various current densities are shown in Figure 3a, which are extracted from their discharge curves (Figure S8a-c, Supporting Information). Evidently, the specific capacity boosts with the increase of the thickness of microelectrode. The HOP Ni@Ni(OH)₂-5.6 yields the highest capacity at all current densities. The same trend is also observed in the specific capacities of S Ni@Ni(OH)₂-X microelectrode, showing apparent lower specific capacities than those of HOP Ni@Ni(OH)₂-X microelectrode. Based on the discharge curves, HOP Ni@Ni(OH)₂-5.6 microelectrode exhibits a maximum capacity of 302.9 μA h cm⁻² at 1 mA cm⁻², which is almost 8.4 times of the maximum capacity of S Ni@Ni(OH)₂-5.6 microelectrode. At a high current density

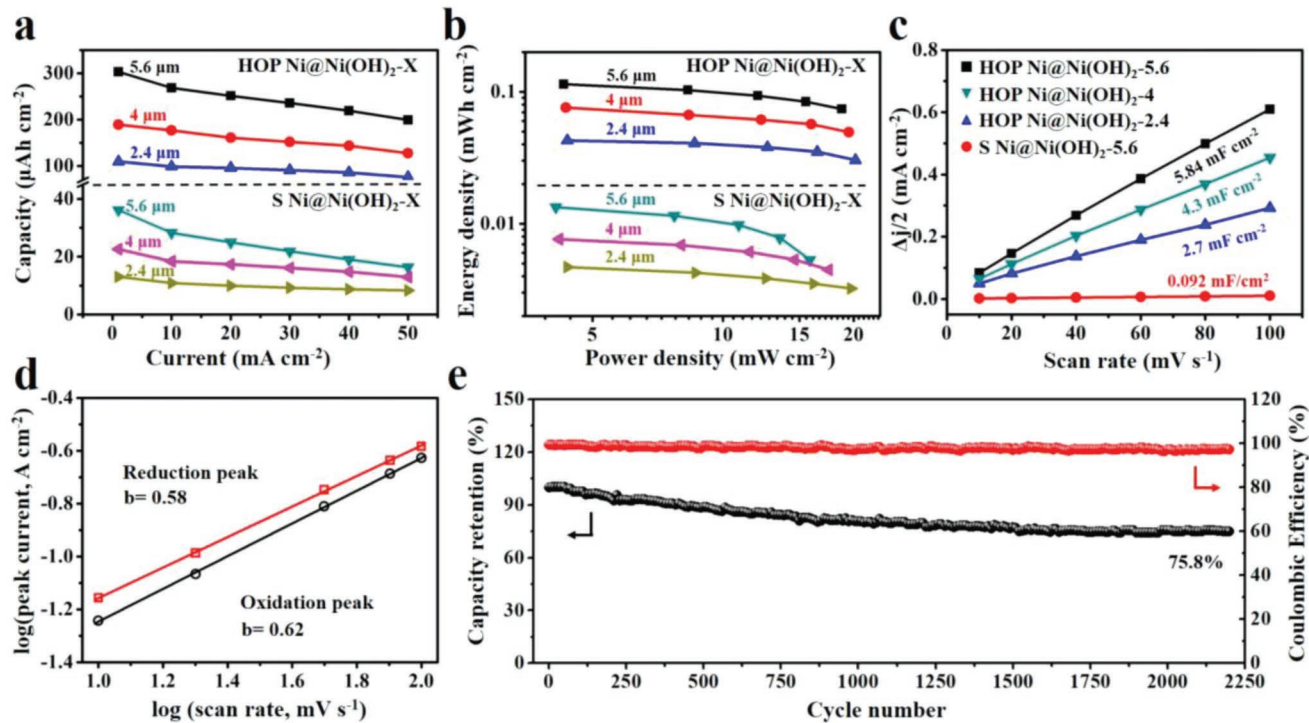


Figure 3. a) Area capacities of HOP Ni@Ni(OH)₂-X and S Ni@Ni(OH)₂-X microelectrodes at various current densities. b) Ragone plots of HOP Ni@Ni(OH)₂-X and S Ni@Ni(OH)₂-X microelectrodes based on the area of microelectrodes. c) Capacitive current densities of HOP Ni@Ni(OH)₂-X and S Ni@Ni(OH)₂-5.6 microelectrodes versus the scan rates and corresponding C_{dl} values estimated through the linear fitting of the plots. d) Peak current densities as a function of scan rates in double logarithmic plot. e) Long-term cycling performance and corresponding Coulombic efficiency of the aqueous HOP Ni@Ni(OH)₂-5.6 microelectrode at a current density of 20 mA cm⁻².

of 50 mA cm⁻², much higher capacity retention (65.81%) is obtained by HOP Ni@Ni(OH)₂-5.6 microelectrode, implying its excellent rate performance. In contrast, the S Ni@Ni(OH)₂-5.6 microelectrode only delivers a low capacity retention of 45.19% at the same current density. Furthermore, the capacity retention of S Ni@Ni(OH)₂-2.4 microelectrode and S Ni@Ni(OH)₂-4 microelectrode are 57.24% and 63.48%, respectively. Obviously, the increase in the thickness of S Ni@Ni(OH)₂-X microelectrode results in a worse rate performance. The ion transport on the surface of the material and in the electrolyte is hindered by the less, complex and lengthy ion transport paths. By comparison, the disparity among the capacity retention of HOP Ni@Ni(OH)₂-2.4 (71.34%), HOP Ni@Ni(OH)₂-4 (67.48%) and HOP Ni@Ni(OH)₂-5.6 (65.81%) is negligible, which is attributed to the shortened pathway for ion transport and charge transfer provided by HOP structure.

Additionally, the areal energy/power densities of HOP Ni@Ni(OH)₂-X and S Ni@Ni(OH)₂-X microelectrodes were further investigated (Figure 3b). Although the energy/power densities of HOP Ni@Ni(OH)₂-X and S Ni@Ni(OH)₂-X microelectrodes make no sense when compared with the energy/power densities of full cells in other reports. In the same reaction system and conditions in this work, the energy/power densities calculated from the cathode discharge can be compared qualitatively. It is obvious that the HOP Ni@Ni(OH)₂-X microelectrodes deliver the higher areal energy/power densities than those of S Ni@Ni(OH)₂-X microelectrodes. For HOP Ni@Ni(OH)₂-X microelectrodes, with the increase of microelectrode thickness, energy density shows an ascending trend with a weeny wastage in power densities (7.03%). By contrast, S Ni@Ni(OH)₂-5.6 microelectrode yields an inferior power density retention (19.61%) with the microelectrode thickness ranging from 2.4 to 5.6 μm. It demonstrates that high energy/power densities and rate capability can be realized simultaneously in these HOP microelectrodes.

To evaluate the electrochemically active surface area (ECSA) of HOP Ni@Ni(OH)₂-X and S Ni@Ni(OH)₂-5.6 microelectrodes, which are proportional to the electrochemical double layer capacitance (C_{dl}), a series of CV tests at different scan rates in the potential ranging from 0.15 to 0.25 V versus Hg/HgO were carried out. All CV curves of HOP Ni@Ni(OH)₂-X and S Ni@Ni(OH)₂-5.6 microelectrodes show a typically rectangular feature (Figure S9, Supporting Information). HOP Ni@Ni(OH)₂-X microelectrode exhibits a larger current density compared with S Ni@Ni(OH)₂-5.6 microelectrode at the same scan rate. The C_{dl} is equal to the linear slope of the plot of the corresponding different current densities (j) versus different scan rates (Figure 3c). The C_{dl} of HOP Ni@Ni(OH)₂-5.6 microelectrode is calculated to be 5.84 mF cm⁻², which is approximately 62.5 times higher than that of S Ni@Ni(OH)₂-5.6 microelectrode. In addition, the C_{dl} of HOP Ni@Ni(OH)₂-2.4 microelectrode and HOP Ni@Ni(OH)₂-4 microelectrode are 2.7 and 4.3 mF cm⁻², respectively. Obviously, for HOP Ni@Ni(OH)₂-X, the increase of C_{dl} is proportional to the increase of thickness. The higher C_{dl} value implies a higher ECSA and indicates more active sites of microelectrode, which results in the enhanced capacity.

In order to get better understanding of the charge storage kinetics of the HOP Ni@Ni(OH)₂-5.6 microelectrode, the relationships of the oxidation/reduction peak current densities (i)

versus scan rates (v) are investigated in double logarithmic scale (Figure 3d). The oxidation/reduction peak current densities are obtained from Figure S7 in the Supporting Information. Both plots depict a linear relationship, and the slopes of oxidation/reduction peaks are 0.62 and 0.58, respectively. It suggests that the reaction is mainly controlled by ion diffusion.^[14c,17] The cycling performance of HOP Ni@Ni(OH)₂-5.6 microelectrode was further investigated (Figure 3e). A high capacity retention (75.8% after 2200 cycles at 20 mA cm⁻²) and Coulombic efficiency (about 99.9%) are achieved. In addition, the shape of charge–discharge curves is nearly no change during the whole process, exhibiting superior long-term durability (Figure S10, Supporting Information). The high reversibility and stability of HOP Ni@Ni(OH)₂-5.6 microelectrode make it a promising cathode for Ni–Zn microbattery.

2.3. Electrochemical Performance of On-Chip Ni–Zn Microbattery

Figure 4a displays the CV curves and the corresponding reaction equations of Zn and HOP Ni@Ni(OH)₂-5.6 microelectrodes in 1 M KOH aqueous electrolyte at 50 mV s⁻¹. The CV curves show a couple of strong redox peaks of each electrode. Since there is a large redox potential separation between Zn microelectrode and HOP Ni@Ni(OH)₂-5.6 microelectrode, a Ni–Zn MB with high output voltage can be expected. As a consequence, a Ni–Zn MB based on HOP Ni@Ni(OH)₂-5.6 microelectrode (denoted as HOP Ni–Zn MB) was assembled with an aqueous electrolyte (6 M KOH saturated with ZnO). The CV curves of HOP Ni–Zn MB show two redox peaks with the analogous shape at various scan rates, revealing high-rate capability and highly reversible redox reaction (Figure 4b). The two peaks can be ascribed to the following electrochemical reaction: 2 Ni(OH)₂ + Zn(OH)₂ ⇌ Zn + 2 NiOOH + 2 H₂O. Besides, the Ni–Zn MB using S Ni@Ni(OH)₂-5.6 microelectrode as a cathode (denoted as S Ni–Zn MB) was also assembled. According to the CV curves (Figure 4b; Figure S11a, Supporting Information), HOP Ni–Zn MB delivers much higher current response than that of S Ni–Zn MB, implying its higher reaction activity. The galvanostatic charge–discharge (GCD) curves of the HOP Ni–Zn MB at different current densities ranging from 1 to 30 mA cm⁻² are shown in Figure 4c, demonstrating charge–discharge plateaus at about 1.82 V/1.74 V. In contrast with the S Ni–Zn MB (Figure S11b, Supporting Information), HOP Ni–Zn MB displays a much lower voltage hysteresis (0.08 V) and longer discharge plateaus, indicating its fast redox process and higher capacity. Moreover, HOP Ni–Zn MB exhibits a much higher capacity (152.13 μA h cm⁻² at 1 mA cm⁻²) and capacity retention (59.8% at 30 mA cm⁻²), while only a relatively low capacity of 17.54 μA h cm⁻² and capacity retention of 41.0% can be achieved by S Ni–Zn MB (Figure 4d). Electrochemical impedance spectroscopy (EIS) test was conducted to better elucidate the improved electrochemical performance. In the Nyquist plot (Figure S12, Supporting Information), the smaller equivalent series resistance and charge-transfer resistance were obtained in HOP Ni–Zn MB, revealing optimized electron transport. Moreover, the slope of the straight line for the HOP Ni–Zn MB is evidently steeper than that of the S Ni–Zn MB, showing a

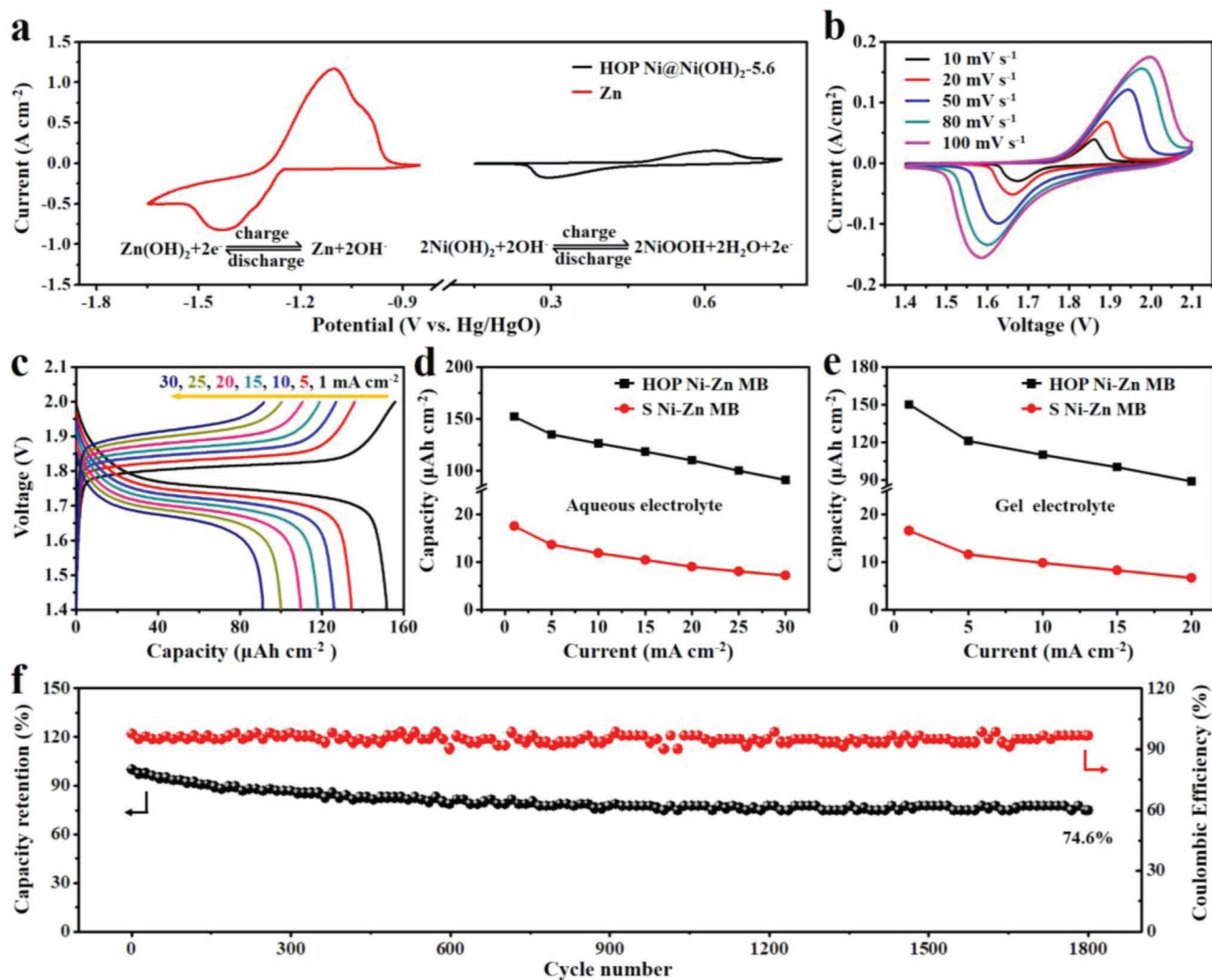


Figure 4. a) CV curves of Zn anode and HOP Ni@Ni(OH)₂-5.6 cathode at 50 mV s⁻¹. b) CV and c) GCD curves of the aqueous HOP Ni-Zn MB. d) Comparison of the rate performance for aqueous HOP Ni-Zn MB and aqueous S Ni-Zn MB. e) Comparison of the rate performance for quasi-solid-state HOP Ni-Zn MB and quasi-solid-state S Ni-Zn MB. f) Long-term cycling performance and corresponding Coulombic efficiency of quasi-solid-state HOP Ni-Zn MB at a current density of 10 mA cm⁻².

much faster ion diffusion rate. The enhanced performances of HOP Ni-Zn MB should be attributed to the optimized ion and electron transport, and increased loading of Ni(OH)₂ provided by the HOP Ni skeleton.

As a demonstration, a quasi-solid-state on-chip Ni-Zn MB was assembled using the same anode and cathode together with polyvinyl alcohol (PVA)-KOH/ZnO gel electrolyte. The Ni-Zn MB shows a slightly increased voltage hysteresis with similar charge-discharge platforms compared with the aqueous HOP Ni-Zn MB (Figure S13, Supporting Information). It is ascribed to higher ion transport and charge transfer resistances of the quasi-solid-state electrolyte, as displayed in EIS (Figure S14, Supporting Information). In addition, the discharge curves reveal a high output voltage of about 1.75 V, which is further determined by a digital avometer (Figure S15, Supporting Information). The high-rate performances of the quasi-solid-state HOP Ni-Zn MB and quasi-solid-state S Ni-Zn MB were

further evaluated and presented in Figure 4e. Interestingly, the quasi-solid-state HOP Ni-Zn MB delivers a high capacity of 150.1 μA h cm⁻² at 1 mA cm⁻², which is nearly equivalent to the capacity of aqueous HOP Ni-Zn MB. It indicates an excellent penetration of the gel electrolyte can be achieved in HOP Ni@Ni(OH)₂ microelectrodes, which is attributed to the interconnected ordered electrolyte-filled macropore-mesopore network. Evidently, the quasi-solid-state HOP Ni-Zn MB achieves a higher capacity of 88.9 μA h cm⁻² at 20 mA cm⁻² and capacity retention (59.2%) than those of the quasi-solid-state S Ni-Zn MB (6.65 μA h cm⁻² and 40.3%), implying its superior rate performance. Furthermore, the cycling performance of quasi-solid-state HOP Ni-Zn MB was investigated in 10 mA cm⁻². The charge-discharge curves of quasi-solid-state HOP Ni-Zn MB are almost unchanged (Figure S16, Supporting Information), and a high retention (74.6% after 1800 cycles) are obtained, revealing excellent long-term cycling stability (Figure 4f).

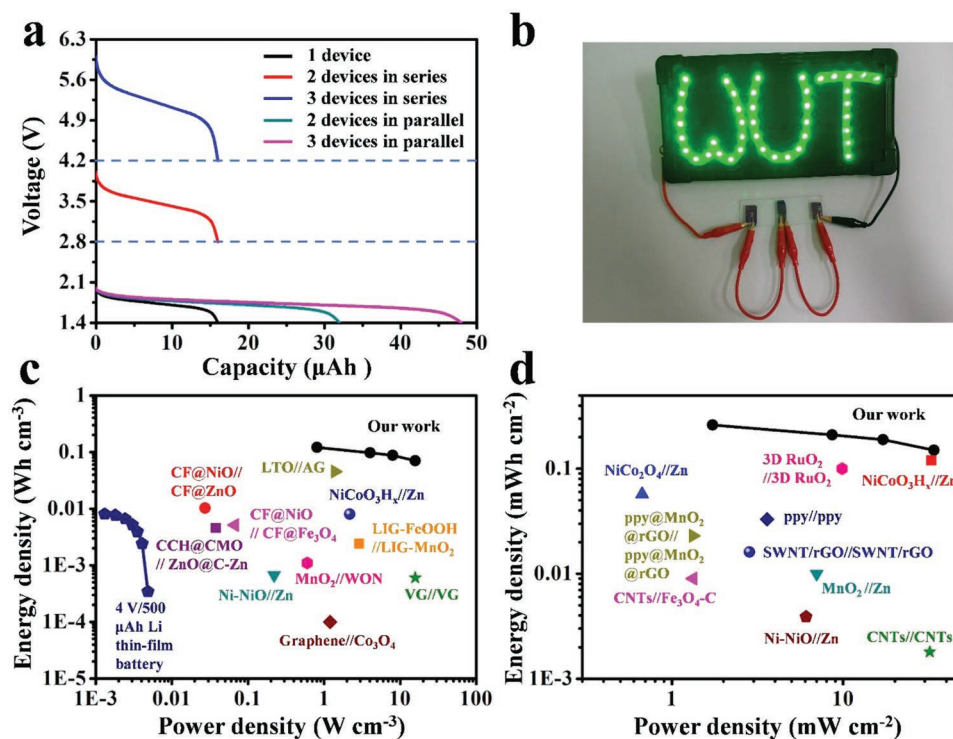


Figure 5. a) GCD curves of MBs connected in series and parallel. b) Digital images showing that three MBs can light a neon sign consisting of 42 LEDs. Ragone plots of quasi-solid-state on-chip Ni–Zn MB based on c) the volumetric energy/power densities, and d) the areal energy/power densities.

In order to investigate the ability of assembling integrated system, the quasi-solid-state HOP Ni–Zn MBs were further assembled in different ways. The discharge curves of a single MB, two MBs, and three MBs in series or in parallel are shown in **Figure 5a**. A twofold wider voltage window (2.8–4 V) and a threefold wider voltage window (4.2–6 V) were achieved by two-series MBs and three-in-series MBs, respectively. In the same manner, a twofold capacity and a threefold capacity were obtained by two-in-parallel MBs and three-in-parallel MBs, suggesting a good performance scalability. Furthermore, to display the practical potential of this quasi-solid-state HOP Ni–Zn MBs, a neon sign consisting of 42 light emission diodes (LEDs) is effectively powered by three-in-series MBs (**Figure 5b**). **Figure 5c,d** depict the Ragone plots comparing the volumetric/areal energy and power densities of this quasi-solid-state HOP Ni–Zn MB with other reported microenergy storage devices. For volumetric performance, the maximum volumetric energy/power densities of 0.12 W h cm⁻³ and 15.8 W cm⁻³ are obtained by quasi-solid-state HOP Ni–Zn MB, which are considerably superior to most recently reported microenergy storage devices (**Figure 5c**; **Table S1**, Supporting Information). For areal performance, the quasi-solid-state HOP Ni–Zn MB delivers an excellent areal energy density of 0.26 mW h cm⁻², much higher than those of most recently reported microenergy storage devices, such as NiCo₃H_x//Zn (0.15 mW h cm⁻²),^[18] NiCo₂O₄//Zn (0.057 mW h cm⁻²),^[16a] MnO₂//Zn (0.01 mW h cm⁻²),^[19] Ni–NiO//Zn (0.0039 mW h cm⁻²),^[14d] etc. Impressively, a maximum power density of 33.8 mW cm⁻² is also achieved by our MB, even higher than many recently reported microsupercapacitors (MSCs), such as carbon nanotubes (CNTs) (32 mW cm⁻²),^[20] 3D RuO₂

(9.87 mW cm⁻²),^[21] polypyrrole (PPy) (3.6 mW cm⁻²),^[22] single walled carbon nanotube (SWCNT)/rGO (2.84 mW cm⁻²),^[23] etc. The details are listed in **Table S2** in the Supporting Information.

3. Conclusion

In summary, a quasi-solid-state on-chip Ni–Zn MB is demonstrated based on the interdigital HOP Ni@Ni(OH)₂ cathode. Benefiting from the rapid ion transport, high electron conductivity, large surface area, and high loading of Ni(OH)₂ provided by interconnected ordered electrolyte-filled macropore–mesopore network, the quasi-solid-state HOP Ni–Zn MB exhibits an remarkably enhanced capacity (150.1 μA h cm⁻² at 1 mA cm⁻²), superior rate capability (59.2% capacity retention at 20 mA cm⁻²), and prominent long-term stability (74.6% capacity retention after 1800 cycles). Furthermore, the quasi-solid-state HOP Ni–Zn MB delivers an impressive energy density (0.26 mW h cm⁻², 0.12 Wh cm⁻³) and power density (33.8 mW cm⁻², 15.8 W cm⁻³), which are obviously superior to most of reported microenergy storage devices. Considering the combined high energy and power densities, our work may provide new direction into high-performance and highly safe microenergy storage units for next-generation highly integrated electronic devices.

4. Experimental Section

Synthesis of PS Microspheres: Monodispersed PS microspheres were synthesized by emulsifier-free emulsion polymerization.^[24] Typically, styrene was washed with an aqueous solution of NaOH (0.1 M) and

deionized (DI) water three times to remove the inhibitor. Afterward, the mixed reaction solution of styrene (10 mL), ethanol (40 mL), sodium dodecyl sulfate (15 mg), and DI water (100 mL) was heated to 70 °C in a three-necked round-bottomed flask. The reaction solution was deoxygenated by continuous bubbling of pure N₂ and stirring with a Teflon paddle. When the temperature of the solution gradually increased to 70 °C, potassium persulfate (20.2 mg) was added. The mixture was kept at 70 °C for 10 h under constant stirring and nitrogen bubbling. When the reaction system was naturally cooled down to room temperature, the PS microspheres with diameters of 180 nm were obtained.

Microfabrication of HOP Ni@Ni(OH)₂-X and S Ni@Ni(OH)₂-X Microelectrode: The interdigital Ti/Au current collectors were obtained on a Si/SiO₂ substrate via photolithography and physical vapor deposition. The thicknesses of Ti and Au are 5 and 145 nm, respectively. For HOP Ni@Ni(OH)₂-X microelectrode, a HOP Ni skeleton on the Ti/Au current collector was achieved through a colloidal templating strategy. Briefly, the synthesized PS microspheres were dispersed in DI water to obtain a suspension with a concentration of 0.25 wt%. The substrates were positioned vertically into vials containing the suspension of PS microspheres at 30 °C. During evaporation, the PS microspheres were self-assembled onto the substrate to form a template with highly ordered face-centered cubic in structure. To enhance the contact between PS microspheres, the substrates were baked at 70 °C for 2 h. Subsequently, Ni was electrodeposited through the template in a commercial electroplating solution. In the electrodeposition process, when the thickness of the nickel electrode exceeded 5.6 μm, in addition to the longitudinal growth, nickel also began to exhibit significant lateral growth, making it difficult to accurately calculate the footprint of the electrode. Therefore, the highest electrode thickness was chosen to be 5.6 μm. HOP Ni@Ni(OH)₂-X microelectrode (X = 2.4, 4, and 5.6) corresponded to the time for electrodeposition of Ni (300, 500, and 700 s, respectively). After removing the PS microspheres by soaking the plated substrates in methylbenzene, the HOP Ni skeletons were obtained. Finally, the Ni(OH)₂ shell was in situ formed by anodizing the surface of HOP Ni skeletons in 1 M KOH aqueous solution at 0.2 A cm⁻² for 18 h. For comparison, the S Ni@Ni(OH)₂-X microelectrodes were obtained by anodizing the surface of planar Ni microelectrodes in 1 M KOH aqueous solution at 0.2 A cm⁻² for 18 h. The planar Ni microelectrodes were fabricated by direct electrodeposition of Ni onto the interdigital Ti/Au current collectors at -20 mA cm⁻² for 400, 600, and 800 s. S Ni@Ni(OH)₂-X microelectrode (X = 2.4, 4, 5.6) corresponded to the time for the electrodeposition of Ni (400, 600, and 800 s, respectively).

Microfabrication of Zn Microelectrode: The Zn microelectrodes were obtained via a facile electrodeposition of Zn on the interdigital Ti/Au current collectors. The electrodeposition was performed at -20 mA cm⁻² for 30 min in an aqueous electroplating solution (0.5 M ZnSO₄ and 0.5 M NaSO₄).

Material Characterization: The SEM images of the samples were observed by a JEOL JSM-7100F scanning electron microscope. EDS were collected by an Oxford IE250 system. TEM images were collected using Titan G2 60300 Probe Cs Corrector HRSTEM. X-ray diffractometer characterizations were collected using a D8 Discover X-ray diffractometer with Cu Kα radiation (λ = 1.054056 Å). XPS measurements were performed with a VG MultiLab 2000 instrument. The thicknesses of microelectrodes were measured by stylus surface profiler (Bruker Dektak TX).

Electrochemical Measurements: The electrochemical measurements were conducted using a CHI 760E electrochemical workstation (CH Instruments, China) at room temperature. For three-electrode system tests, HOP Ni@Ni(OH)₂-X microelectrode or S Ni@Ni(OH)₂-X microelectrode was directly used as the working electrode. A Pt plate and a Hg/HgO electrode were used as the counter electrode and the reference electrode, respectively. 1 M KOH was used as the electrolyte. The electrochemical performances of Ni-Zn MB were investigated in a two-electrode system, in which the HOP Ni@Ni(OH)₂-X or S Ni@Ni(OH)₂-X used as the cathode and Zn microelectrode were directly

used as anode. The PVA-KOH/ZnO gel electrolyte was obtained by dissolving 3 g PVA in 30 mL DI water under stirring at 85 °C for 3 h. Thereafter, 10 mL aqueous solution (6 M KOH saturated with ZnO) was added slowly into the well-dissolved PVA solution under vigorous stirring. After the electrolyte was solidified, a quasi-solid-state on-chip Ni-Zn MB was attained. EIS measurements were carried out by applying an AC voltage of 5 mV amplitude with a frequency ranging from 0.01 Hz to 100 kHz at open circuit potential.

Supporting Information

Supporting Information is available from the Wiley Online Library or from the author.

Acknowledgements

This work was supported by the National Natural Science Fund for Distinguished Young Scholars (51425204), the National Natural Science Foundation of China (51832004, 51502227, 51579198, and 51802239), the National Key R&D Program of China (2016YFA0202604), the Yellow Crane Talent (Science & Technology) Program of Wuhan City and Wuhan Morning Light Plan of Youth Science and Technology (No. 2017050304010316), L.H. gratefully acknowledged financial support from China Scholarship Council (No. 201606955094).

Conflict of Interest

The authors declare no conflict of interest.

Keywords

aqueous rechargeable batteries, energy storage, high energy density, high power density, microdevices

Received: November 28, 2018

Revised: February 12, 2019

Published online: February 25, 2019

- [1] a) N. Choudhary, C. Li, J. Moore, N. Nagaiah, L. Zhai, Y. Jung, J. Thomas, *Adv. Mater.* **2017**, *29*, 1605336; b) M. R. Lukatskaya, D. Bruce, G. Yury, *Nat. Commun.* **2016**, *7*, 12647.
- [2] a) W. Liu, M. S. Song, B. Kong, Y. Cui, *Adv. Mater.* **2017**, *29*, 1603436; b) M. Beidaghi, Y. Gogotsi, *Energy Environ. Sci.* **2014**, *7*, 867; c) L. Wen, F. Li, H. M. Cheng, *Adv. Mater.* **2016**, *28*, 4306.
- [3] a) J. Deng, X. Lu, L. Liu, L. Zhang, O. G. Schmidt, *Adv. Energy Mater.* **2016**, *6*, 1600797; b) X. Li, M. Gu, S. Hu, R. Kennard, P. Yan, X. Chen, C. Wang, M. J. Sailor, J. G. Zhang, J. Liu, *Nat. Commun.* **2014**, *5*, 4105; c) E. Eustache, P. Tilmant, L. Morgenroth, P. Roussel, G. Patriarche, D. Troadec, N. Rolland, T. Brousse, C. Lethien, *Adv. Energy Mater.* **2014**, *4*, 1079.
- [4] a) D. Li, R. Cheng, H. Zhou, C. Wang, A. Yin, Y. Chen, N. O. Weiss, Y. Huang, X. Duan, *Nat. Commun.* **2015**, *6*, 7509; b) L. Liu, Q. Weng, X. Lu, X. Sun, L. Zhang, O. G. Schmidt, *Small* **2017**, *13*, 1701847.
- [5] a) X. Wang, X. Lu, B. Liu, D. Chen, Y. Tong, G. Shen, *Adv. Mater.* **2015**, *45*, 4763; b) Y. H. Kwon, S. W. Woo, H. R. Jung, H. K. Yu, K. Kim, B. H. Oh, S. Ahn, S. Y. Lee, S. W. Song, J. Cho, H. C. Shin, *Adv. Mater.* **2012**, *24*, 5145; c) M. Koo, K. I. Park, S. H. Lee, M. Suh, D. Y. Jeon, J. W. Choi, K. Kang, K. J. Lee, *Nano Lett.* **2012**, *12*, 4810.
- [6] A. Patil, V. Patil, W. S. Dong, J. W. Choi, D. S. Paik, S. J. Yoon, *Mater. Res. Bull.* **2008**, *43*, 1913.

- [7] a) G. Nyström, A. Marais, E. Karabulut, L. Wågberg, Y. Cui, M. M. Hamed, *Nat. Commun.* **2015**, *6*, 7259; b) S. R. Gowda, A. L. Reddy, X. Zhan, H. R. Jafry, P. M. Ajayan, *Nano Lett.* **2012**, *12*, 1198; c) H. Ning, J. H. Pikul, R. Zhang, X. Li, S. Xu, J. Wang, J. A. Rogers, W. P. King, P. V. Braun, *Proc. Natl. Acad. Sci. USA* **2015**, *112*, 6573; d) D. Golodnitsky, M. Nathan, V. Yufit, E. Strauss, K. Freedman, L. Burstein, A. Gladkikh, E. Peled, *Solid State Ionics* **2006**, *177*, 2811.
- [8] a) J. F. M. Oudenhoven, L. Baggetto, P. H. L. Notten, *Adv. Energy Mater.* **2011**, *1*, 10; b) S. Ferrari, M. Loveridge, S. D. Beattie, M. Jahn, R. J. Dashwood, R. Bhagat, *J. Power Sources* **2015**, *286*, 25.
- [9] B. Y. Park, L. Taherabadi, C. Wang, Y. Yeh, *J. Power Sources* **2008**, *178*, 795.
- [10] P. L. Taberna, S. Mitra, P. Poizot, P. Simon, J. M. Tarascon, *Nat. Mater.* **2006**, *5*, 567.
- [11] a) J. H. Pikul, Z. H. Gang, J. Cho, P. V. Braun, W. P. King, *Nat. Commun.* **2013**, *4*, 1732; b) H. Zhang, X. Yu, P. V. Braun, *Nat. Nanotechnol.* **2011**, *6*, 277.
- [12] a) Y. Chen, X. Li, K. Park, J. Song, J. Hong, L. Zhou, Y. W. Mai, H. Huang, J. B. Goodenough, *J. Am. Chem. Soc.* **2013**, *135*, 16280; b) Y. Liu, A. A. Elzatahry, W. Luo, K. Lan, P. Zhang, J. Fan, Y. Wei, C. Wang, Y. Deng, G. Zheng, F. Zhang, Y. Tang, L. Mai, D. Zhao, *Nano Energy* **2016**, *25*, 80; c) Q. Wei, Q. An, D. Chen, L. Mai, S. Chen, Y. Zhao, K. M. Hercule, L. Xu, A. Minhas-Khan, Q. Zhang, *Nano Lett.* **2014**, *14*, 1042.
- [13] a) J. F. Parker, C. N. Chervin, I. R. Pala, M. Machler, M. F. Burz, J. W. Long, D. R. Rolison, *Science* **2017**, *356*, 415; b) J. M. Tarascon, M. Armand, *Nature* **2001**, *414*, 359; c) H. Zhou, *Energy Environ. Sci.* **2013**, *6*, 2256; d) Y. Zhao, X. Li, B. Yan, D. Xiong, D. Li, S. Lawes, X. Sun, *Adv. Energy Mater.* **2016**, *6*, 1502175; e) L. Qu, G. Sun, X. Jin, H. Yang, J. Gao, *J. Mater. Chem. A* **2018**, *6*, 10926; f) R. Trócoli, A. Morata, M. Fehse, M. Stchakovsky, A. Sepúlveda, A. Tarancón, *ACS Appl. Mater. Interfaces* **2017**, *9*, 32713.
- [14] a) L. Suo, O. Borodin, W. Sun, X. Fan, C. Yang, F. Wang, T. Gao, Z. Ma, M. Schroeder, C. A. Von, S. M. Russell, M. Armand, A. Angell, K. Xu, C. Wang, *Angew. Chem.* **2016**, *128*, 7252; b) J. Liu, C. Guan, C. Zhou, Z. Fan, Q. Ke, G. Zhang, C. Liu, J. Wang, *Adv. Mater.* **2016**, *28*, 8732; c) Y. Zeng, Y. Meng, Z. Lai, X. Zhang, M. Yu, P. Fang, M. Wu, Y. Tong, X. Lu, *Adv. Mater.* **2017**, *29*, 1702698; d) R. Wang, Y. Han, Z. Wang, J. Jiang, Y. Tong, X. Lu, *Adv. Funct. Mater.* **2018**, *28*, 1802157; e) M. A. González, R. Trócoli, I. Pavlovic, C. Barriga, F. L. Mantia, *Electrochem. Commun.* **2016**, *68*, 1.
- [15] a) Z. Tang, C. H. Tang, H. Gong, *Adv. Funct. Mater.* **2012**, *22*, 1272; b) J. Yan, Z. Fan, S. Wei, G. Ning, W. Tong, Z. Qiang, R. Zhang, L. Zhi, W. Fei, *Adv. Funct. Mater.* **2012**, *22*, 2632.
- [16] a) C. Xu, J. Liao, C. Yang, R. Wang, D. Wu, P. Zou, Z. Lin, B. Li, F. Kang, C. P. Wong, *Nano Energy* **2016**, *30*, 900; b) Y. Z. Su, K. Xiao, N. Li, Z. Q. Liu, S. Z. Qiao, *J. Mater. Chem. A* **2014**, *2*, 13845.
- [17] a) H. S. Kim, J. B. Cook, H. Lin, J. S. Ko, S. H. Tolbert, V. Ozolins, B. Dunn, *Nat. Mater.* **2016**, *16*, 454; b) M. Fehse, R. Trócoli, E. Ventosa, E. Hernández, A. Sepúlveda, A. Morata, A. Tarancón, *ACS Appl. Mater. Interfaces* **2017**, *9*, 5295.
- [18] Y. Huang, W. S. Ip, Y. Y. Lau, J. Sun, Z. Jie, N. S. S. Yeung, W. S. Ng, H. Li, Z. Pei, Q. Xue, Y. Wang, J. Yu, H. Hu, C. Zhi, *ACS Nano* **2017**, *11*, 8953.
- [19] Y. Zeng, X. Zhang, Y. Meng, M. Yu, J. Yi, Y. Wu, X. Lu, Y. Tong, *Adv. Mater.* **2017**, *29*, 1700274.
- [20] J. Ren, W. Bai, G. Guan, Y. Zhang, H. Peng, *Adv. Mater.* **2013**, *25*, 5965.
- [21] A. Ferris, S. Garbarino, D. Guay, D. Pech, *Adv. Mater.* **2016**, *27*, 6625.
- [22] L. Yuan, B. Yao, B. Hu, K. Huo, W. Chen, J. Zhou, *Energy Environ. Sci.* **2013**, *6*, 470.
- [23] D. Yu, K. Goh, H. Wang, L. Wei, W. Jiang, Q. Zhang, L. Dai, Y. Chen, *Nat. Nanotechnol.* **2014**, *9*, 555.
- [24] J. Cai, M. Wu, Y. Wang, H. Zhang, M. Meng, Y. Tian, X. Li, J. Zhang, L. Zheng, J. Gong, *Chem* **2017**, *2*, 877.